Rover Mobility in a Lunar Analogue Dataset

Bailey C. Hopkins*, Ryan Hartzell, Ethan J. Paul, Cameron Hinkle, Charles Yuroff,
Christopher Dreyer, Frances Zhu
Department of Mechanical Engineering, Colorado School of Mines
Golden, CO, USA

***Abstract*—Planetary surface missions depend on reliable rover traversability across diverse terrain conditions. Accurate prediction of traversability relies on terramechanics, the study of wheel–soil interactions, which links terrain properties to vehicle dynamics. Building and validating terramechanics-based models require high-fidelity datasets that couple specific rover geometries with well-characterized surface topographies, yet such datasets remain sparse or incomplete. This paper presents a streamlined experimental pipeline for generating and disseminating comprehensive mobility datasets. We describe our rover, test campaigns, and detail the data-acquisition architecture. Additionally, we release a publicly accessible repository of rover state & action time series, wheel imagery, and terrain scans captured in the Mines Lunar Surface Simulator. The dataset and methodology enable rapid development and validation of traversability metrics, digital twin simulation, and system identification.**

***Index Terms*—Rover mobility, Terramechanics, Planetary surface exploration, Open-source datasets**

I. Introduction

Traversability assessment is a critical capability for robotic exploration of planetary surfaces, where mission success depends on a rover's ability to negotiate uncertain and heterogeneous terrain. Terramechanics provides the physical framework linking soil properties, wheel geometry, and operating conditions to resultant forces and torques. Quantitative traversability analysis, therefore, requires empirical data that capture the coupled dynamics of a specific rover operating on a specific surface topography. In practice, however, published mobility datasets are either proprietary, limited in scope, or lack the resolution needed to parameterize and validate high-fidelity models. Researchers seeking to perform rigorous traversability studies must often replicate expensive test campaigns or rely on low-confidence extrapolations.

Our contribution addresses that gap by introducing an end-to-end pipeline for high-resolution mobility data collection and by publishing a complete dataset acquired with the RoSEy CubeRover in the Mines Lunar Surface Simulator (MLSS). The contributions of the paper are threefold. First, a reproducible methodology for synchronously capturing rover dynamics and terrain state, including motion-capture ground truth, onboard telemetry, and overhead LiDAR scans. Second, a curated dataset comprising 1680 controlled trials spanning various velocities, turning radii, and inclinations across lunar simulant. And lastly, an open-source tool for post-processing, visualization, and integration with existing simulation and machine-learning workflows.

The following sections provide background for what information is necessary to characterize rover mobility, the experimental methodology to collect this data, the collected raw data, the final data product.

II. Background

Rover mobility integrates vehicle dynamics, terramechanics, and terrain properties. To generate a physics-derived predictive dynamics model for a rover, previous work by the RoSE Lab [1] shows that the parameters listed in Table I are necessary. These are not all of the parameters that can be collected to define terramechanics; they are, however, the minimum set of parameters needed to generate forces and torques on a rover and propagate the rover state for the use of system identification. Wheel parameters P_W and soil parameters P_S can be determined from the type of rover used and the environment that the rover is traversing on. The running state parameters P_R can be determined from experimentation, and specific sensors need to be selected to acquire these parameters.

TABLE I
Parameters that are needed to conduct a physics-derived predictive dynamics model for rover mobility.

Wheel Parameters P_W		**Soil Parameters P_S**	
Symbol	Definition	Symbol	Definition
r	Wheel radius	ϕ	Internal friction angle
b	Wheel width	c	Soil cohesion
h	Grouser height	ρ	Soil mass density
Running State Parameters P_R			
Symbol	Definition	k'_ϕ	Bekker coefficient of density
v	Wheel linear speed	k'_c	Bekker coefficient of cohesion
ω	Wheel angular speed	n_0	Nominal sinkage exponent
θ_1	Wheel entry angle	n_1	Slip-sinkage exponent
θ_2	Wheel exit angle	K	Shear deformation modulus
z	Wheel sinkage		

This work was supported by the AI Institute in Dynamic Systems, one of the National Artificial Intelligence Research institutes funded by the National Science Foundation (NSF) via award number 2112085, and was supported by a Lunar Surface Technology Research grant from NASA's Space Technology Research Grants Program.

*Corresponding author: bailey_hopkins@mines.edu

Prior work contains some, but not all, of this data. NASA Glenn Research Center and Youngstown State University tested a one-sixth-scale Lunar Electric Rover over a cleat obstacle, publishing high-speed-video-derived chassis and wheel-deflection time-series, but no force, slip, or power telemetry, and the raw files are not publicly archived [2]. Carnegie Mellon University's Scarab field trials reported drawbar pull, percent slip, and slope-traverse performance on granular media; however, only summary values appear in the literature, and neither the underlying slip or power logs nor the associated terrain meshes have been released [3]. Jet Propulsion Laboratory's Mars 2020 traversability trade study combined publicly available orbital imagery with machine-learning terrain classification and speed–slope lookup tables to generate site-wide cost maps and Monte-Carlo traverse-time distributions; the imagery and derived maps are accessible through the Planetary Data System, but the model input tables and simulation outputs are not provided [4]. Consequently, existing sources either lack wheel-by-wheel force or power telemetry, omit co-registered terrain meshes, or remain behind institutional walls, limiting their usefulness for rigorous traversability validation.

The proposed mobility experiment campaign expands the available dataset by providing integrated baseline rover state and action time series that pair detailed wheel telemetry with high-resolution terrain reconstructions across a broad range of speeds, turn radii, and inclinations. The dataset is intended to serve the spectrum of classical physics-based terramechanics studies to modern data-driven methods that benefit from large, labeled mobility datasets.

III. Methodology

This section describes the rover employed in the trials, the testbed, and the mobility experiment procedure. All designs for the mechanical, electrical, and software design of the rover are found at https://github.com/RoSE-Lab-Admin.

A. Rover

The rover in these experiments is the Robotic Space Exploration Lab's (RoSE Lab) CubeRover named RoSEy. The platform adheres to Astrobotic's CubeRover–6U standard, which categorizes platforms into 2U, 4U, and 6U configurations [5]. RoSEy conforms to the 6U specification, with a nominal payload volume of $300\,\mathrm{mm} \times 200\,\mathrm{mm} \times 100\,\mathrm{mm}$ and a total mass of $16\,\mathrm{kg}$, comprising a $10\,\mathrm{kg}$ base and a $6\,\mathrm{kg}$ payload. RoSEy has an operational mass for this dataset of $16.01\,\mathrm{kg}$.

1) Structures: RoSEy is shown in Fig. 1, with her wheel dimensions in Fig. 1. For both the rover chassis and wheel reference frames are described in the corresponding figures. All dimensions and specifications reported here correspond to the configuration employed during mobility trials.

The rover measures $703.7\,\mathrm{mm} \times 422.0\,\mathrm{mm} \times 405.2\,\mathrm{mm}$ (length L $\times$ width W $\times$ height H). The center of mass (COM), referenced to the front–bottom left corner of the bounding box of the rover, is located at

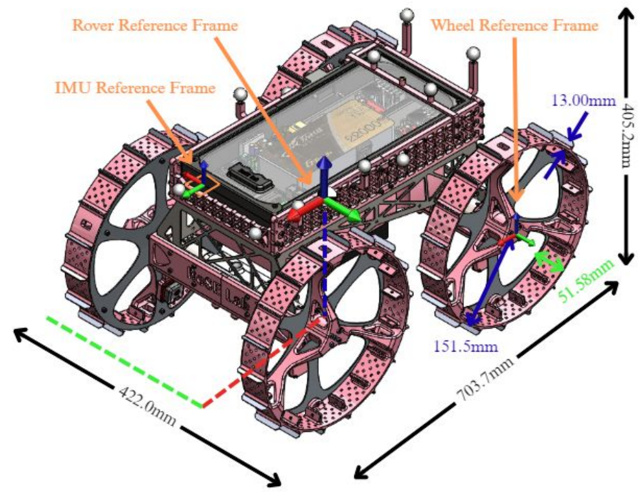

Fig. 1. RoSEy CubeRover–6U dimensions and reference frames for the rover frame, IMU frame, and wheel frame defined in Section IV-C1. Relevant dimensions, such as rover length L $\times$ width W $\times$ height H, the location of the center of mass, wheel radius r, wheel width b, and grouser height h are shown. Axes in all reference frames are color-coded consistently: $\hat{x}$ (red), $\hat{y}$ (green), and $\hat{z}$ (blue).

$(-354.7,\ 210.4,\ 220.9)\,\mathrm{mm}$ in ${}^{R}(L, W, H)$. The inertia tensor, expressed in $\mathrm{kg\,m^2}$ about the COM, is given in (1).

$$
{}^{\mathbf{R}}\mathbf{I} = \begin{bmatrix} 0.1867 & 0.001129 & -0.001983 \\ 0.001129 & 0.3888 & -0.0007294 \\ -0.001983 & -0.0007294 & 0.4366 \end{bmatrix} \ \mathrm{kg\,m^2} \tag{1}
$$

The wheel architecture, shown in Fig. 1, includes an outer rim radius r of $151.5\,\mathrm{mm}$, eighteen evenly spaced grousers with height h of $13.00\,\mathrm{mm}$, and a width b of $51.58\,\mathrm{mm}$. Wheels are mounted to motor shafts via bolted hubs.

Structural components are primarily produced via additive manufacturing, with polylactic acid (PLA) used for the avionics bay, payload bay, motor enclosures, camera mounts, motion-capture marker mounts, and portions of the wheel assemblies. The chassis is laser-cut from mild steel, lids from laser-cut acrylic, and aluminum grousers and wheel backing plates are waterjet-cut. While matching the intended flight design in dimensions, geometry, and mass, the rover's materials and fabrication methods emphasize rapid prototyping, iteration, and cost efficiency, making it unsuitable for spaceflight and intended solely as a terrestrial mobility test platform. Mechanical dust mitigation protects avionics and payloads, with sensitive components in sealed enclosures and interface points designed to block particulate ingress. A modular architecture enables rapid payload integration and component replacement, while brass heat-set inserts secure 3D-printed parts to metallic or removable hardware, ensuring robust, repeatable threaded connections.

2) Avionics: The avionics system (Fig. 2) is powered by a $14.8, \mathrm{V}$, $22,000, \mathrm{mAh}$, four-series (4S), $25, \mathrm{C}$ lithium-polymer (Li-Po) battery. A manual bypass breaker switch interrupts the battery connection, with power routed through

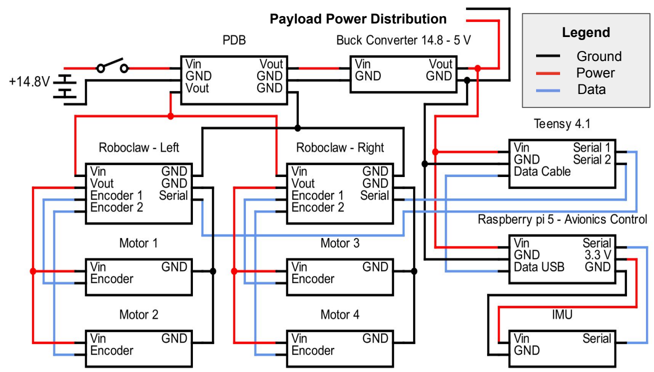

Fig. 2. Avionics power and data distribution architecture for RoSEy. The 14.8 V main supply is routed through a power distribution board (PDB) and a buck converter to provide regulated 5 V for control electronics. Dual Roboclaw motor controllers independently drive left and right motor pairs, each with integrated encoder feedback. Power (red), ground (black), and data (blue) connections link the Raspberry Pi 5 avionics computer, Teensy 4.1 microcontroller, and IMU, enabling coordinated motor control, sensor acquisition, and communication.

a power-distribution board (PDB). The PDB delivers 14.8, V to two Roboclaw 2,×,15 A motor controllers, each driving and reading encoders from two Yellowjacket 5203-series motors—one controller per rover side for skid-steer control.

The PDB also feeds a 20, A buck converter stepping voltage to 5, V for two Raspberry Pi 5 boards and a Teensy 4.1 microcontroller. The primary Raspberry Pi communicates with the Teensy via USB; the Teensy connects to both Roboclaws in active-serial mode. The Raspberry Pi also interfaces with a BNO055 IMU over UART, supplying 3.3, V power.

3) Software and Control: RoSEy's control system uses the primary Raspberry Pi 5 for locomotion and data collection, with both Pi boards running *ROS 2 Jazzy*. The primary avionics computer runs Ubuntu 24.04 LTS, and the wheel camera computer runs Debian 12 "Bookworm". All ROS nodes communicate over a LAN via Fast DDS shown in Fig. 3.

Motor control is managed by the Teensy 4.1, running custom firmware to interface with the Roboclaws. The Teensy receives high-level motion commands via serial from the primary computer and returns motor telemetry packets. ROS 2 action servers on the primary computer publish motion goals—linear velocity, turning radius, and acceleration profiles—relayed to the Teensy through a custom serial bridge.

IMU data is obtained via the open-source BNO055 ROS 2 package on the primary computer. The wheel camera computer uses the `camera_ros` package to initialize cameras and publish images, which are compressed with `cv_bridge`. Relevant topics are recorded with custom rosbag2 nodes, triggered by a service request at test start-up.

B. Testing Environment

All tests were performed in the Colorado School of Mines Lunar Surface Simulator (MLSS) testbed [6]. A digital reconstruction of the MLSS testbed is shown in Fig. 4. In

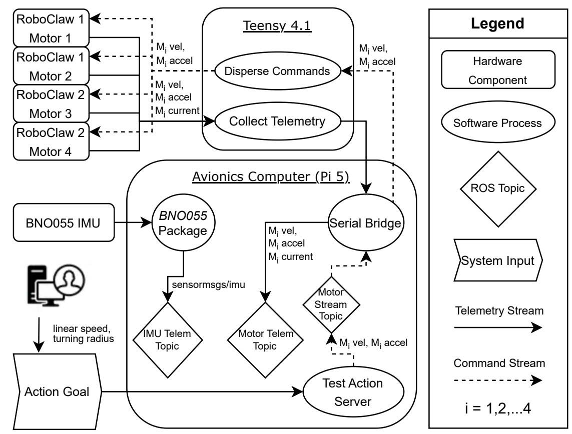

Fig. 3. CubeRover software architecture, which shows the flow of commands of an operator from an action goal to the motor controllers (solid), and how onboard sensor data is collected and published to ROS topics (dashed). M_i refers to the i^{th} motor with $i = 1, 2, 3, 4$.

this section, first, the lunar simulant used and its surface preparation are reviewed. Subsequently, two testbed sensors critical to mobility characterization are described.

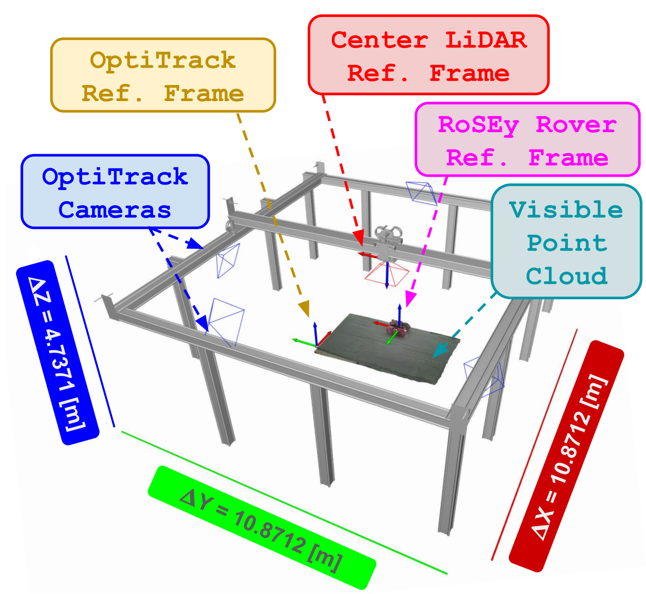

Fig. 4. This digital reconstruction of the MLSS testbed shows the Optitrack PrimeX 22 cameras (blue), the Intel RealSense L515 LiDAR sensor (red), the moveable gantry system, and a pointcloud reconstruction of the prepared surface with the RoSEy rover. The reference frames for the rover frame, OptiTrack frame, and LiDAR frame are also shown at their respective origins. Axes in all reference frames are color-coded consistently: $\hat{x}$ (red), $\hat{y}$ (green), and $\hat{z}$ (blue).

1) Simulant Properties: The simulant used during mobility trials is the Colorado School of Mines - Lunar Highlands Type - Testbed (CSM-LHT-T). Work by Jehn reports the geotechnical properties summarized in Table II, [6].

2) Simulant Preparation: The simulant is prepared between trials to avoid unintended compaction and to improve reproducibility. Depending on the condition of the MLSS

TABLE II
GEOTECHNICAL PROPERTIES OF CSM-LHT-T LUNAR SIMULANT

Property	Value
$\rho_{\min}$	$1.3026\,\mathrm{g/cm^3}$
$\rho_{\max}$	$1.9491\,\mathrm{g/cm^3}$
C_c	0.101
c	10.4–12.5 kPa
ϕ	$20.7°$–$24.7°$

Testbed surface before trials, the authors use one of three methods to prepare the surface.

Surface preparation was conducted using one of three methods, depending on the degree of compaction. Large-scale preparation was only employed after significant compaction, such as from repeated walking, large-scale rover operations, or multiple days without preparation. In this case, a lawn tiller was used to disrupt the regolith and break up clumps, followed by Medium Scale Preparation after the dust settled. Medium-scale preparation, the most common method, was used for surfaces compacted by repeated lightweight rover use and followed Glenn Research Center guidelines [7]. This involved loosening the simulant with a shovel inserted perpendicular to the surface, tilted back to approximately $45°$, and withdrawn, progressing in half-shovel-length increments with 25% lateral overlap, then leveling the surface with a rake. Small-scale preparation was used when little to no compaction was present, consisting of scratching the surface to the depth of a rake's teeth to loosen the top layer and remove tracks, followed by light leveling with a rake.

To ensure that the prepared surface is in view of the Terrain Scanning System, a set of wooden frames provides bounds for the preparation area. These frames are removed during tests of $0°$ inclination to avoid the frames' edge effects. During trials where the inclination $\neq 0°$, the wooden frames remain in place to prevent the regolith from fully collapsing; however, does introduces boundary effects in the terramechanics.

3) Terrain Scanning System: To quantify potential discrepancies in surface level and slope, three Intel RealSense L515 LiDAR sensors capture static overhead scans of the test surface before and after each test. The resulting point clouds are aggregated into derivative products such as tessellated meshes or raster data. A LattePanda 3 Delta computer handles LiDAR data capture via the Intel RealSense SDK and the RealSense ROS 2 wrapper. The LiDARs are calibrated for optical distortions via standard checkerboard methods, resulting in both camera intrinsics and distortion coefficients.

For calibration and noise characterization, the ChArUco calibration board is mounted to a long section of 80/20 aluminum T-Frame rail, and the mount points are fitted with Optitrack passive motion trackers, all measured relative to identifiable features on the ChArUco calibration board. A rigid body is constructed in the Optitrack Motive software, and a pose stream for the calibration plate is captured simultaneously during a long 30-second lidar scan with the calibration plate in the lidar field of view. Specific transforms constructed are available in Eq. 8.

4) Motion Capture System: Four OptiTrack PrimeX 22 cameras are mounted around the MLSS to capture extrinsic pose data. OptiTrack Motive 3.1 software records positions and quaternion orientations of targets when active. Passive markers attached to RoSEy define a rigid body and can be seen in Fig. 1, allowing real-time tracking.

C. Experiment Campaign

For a given day of trials, the authors first prepared the MLSS Testbed as outlined in Section III-B2. The authors then determined the trial parameters that needed to be varied and would conduct and run trials until there was no more usable space on the testbed. Each trial varied the rover's velocity, turning radius, inclination, or a combination of these parameters.

The parameter set that is being varied in this study can be seen in Table III. The velocity of the rover ranges from 1 cm/s to 10 cm/s in 1 cm/s increments to capture the full velocity capabilities of RoSEy. The turning radius ranges from 0 cm (in-place spin) to 120 cm in 20 cm increments, additionally, a turning radius of ∞ cm/s means that the rover is traveling in a straight line. Each radius was tested in clockwise and counterclockwise directions. The last parameter to vary is the inclination, which ranges from $-30°$ (downhill) to $30°$ (uphill) in $5°$ increments. During a single trial, the authors could vary any of these variables to make a trial that captured specific motion. Due to space limitations in the MLSS Testbed, it was not possible to capture changes in turning radius and inclination; thus, all trials with a finite turning radius were conducted at an inclination of $0°$. Future additions to this experiment campaign include testing the combination of inclination and turning radius, as well as transitional states such as traveling between a level surface and inclination.

TABLE III
PARAMETER SWEEPS FOR THE EXPERIMENT CAMPAIGN

Parameter	Values	Levels
Velocity	$[1, 2, 3, 4, 5, 6, 7, 8, 9, 10]$ cm/s	10
Turning radius	$[0, 20, 40, 60, 80, 100, 120, \infty]$ cm	8
Inclination	$[0, \pm5, \pm10, \pm15, \pm20, \pm25, \pm30]\,°$	13

For every trial, the rover followed the sequence outlined below, where phases are bolded, the length of the phase is in parentheses, and a description of the phases follows:

- **Initial padding** (20 s): the rover remained stationary while data logging started, ensuring all systems were recording. An initial LiDAR scan of the surface was captured.
- **Wind-up** (5 s): the rover accelerated linearly from rest to its target speed or turn rate.

- **Steady driving**: the rover maintained the target speed, turning radius, & slope while all data streams were recorded. Due to limitations in testing, this time was set to 15 s for trials with nonzero inclination.
- **Wind-down** (5 s): the rover decelerated to a stop.
- **Final padding** (20 s): the rover remained stationary to ensure complete data capture. A second LiDAR scan was captured.

To ensure that enough data was collected for each parameter set to capture variability, each test was repeated so that 240 s of wind-up, steady driving, and wind-down data was collected. Trials with 0 inclination & no turning were repeated 6 times. Trials with 0 inclination but finite turning radii were repeated with 3 counter-clockwise turns and 3 clockwise turns. All trials with a nonzero inclination were repeated 10 times. The total number of attempted individual trials was 1680. During data collection, it was observed that RoSEy would flip when attempting to climb slopes of 25°. Data for this "failure" area were recorded and are undergoing additional analysis.

IV. Results & Data Presentation

This section summarizes the dataset organization, raw ROS 2 telemetry, and the processing pipeline that produces data in the unified trial frame for analysis. Storage distinguishes valid trials from retained but incomplete data. Coordinate frames and a consistent transformation chain synchronize signals, downsample to the least sampled stream, remove bias and noise when appropriate, and express all measurements in a path-aligned frame with the initial rover heading along $+\hat{\mathbf{x}}$. A trial output is included showing state time series, action time series, and pre-trial and post-trial LiDAR terrain maps.

A. Dataset Storage Architecture

Within the open dataset, the top-level directory is the `Database`, which contains two collections, `Trial_Data` and `Off_Nominal_Data`. Under `Trial_Data`, experiments are grouped by configuration in folders named `Speed_Radius_Direction_Inclination`. Each configuration folder contains per-trial subfolders `Trial_i` for repetitions $i = 1, \ldots, n$. Inside each `Trial_i` folder there is a `Raw_Data` directory holding the original sensor bag files, specifically LiDAR, camera, motion capture, IMU, and motor encoder logs, and a single `Processed_Data.csv` that aggregates the sensor streams after down sampling to the least sampled stream and expresses all signals in the trial frame. Trials where data is incomplete are retained under `Off_Nominal_Data` for completeness. Researchers who use the dataset are requested to cite this paper. Due to the large size of the dataset, a GitHub public repository that holds the description of the dataset, change logs of the data, and how to access the data can be accessed at https://github.com/RoSE-Lab-Admin/Rover-Mobility-Dataset

B. Raw Data

All telemetry was recorded as ROS 2 messages for portability, synchronization, and post-processing. For each data type, the estimated file size is included. With the given estimates for file size, each trial makes a file ≈ 1.8 GB, and a total data set of ≈ 3 TB.

1) Onboard IMU: A BNO055 IMU recorded 4 degrees of freedom quaternion orientation, 3 degrees of freedom angular velocity, and 3 degrees of freedom linear acceleration at ≈ 100 Hz, giving a file size of ≈ 2 MB. The onboard IMU data is used as a secondary monitoring system for the position and orientation of the rover, and for collecting rover speed v.

2) Onboard Motor Data: Each motor of the 4 motor encoder provided wheel position and wheel angular velocity. This data was recorded at a rate of $\approx$ 10 Hz, giving a file size of $\approx$ 80 KB. The onboard motor encoder data gives the authors the wheel angular speed ω.

3) Onboard Wheel Cameras: Four RGB cameras mounted beneath the rover viewed each wheel. The cameras recorded at 960 $\times$ 540 pixels and $\approx$ 15 fps, giving a file size of $\approx$ 450 MB. The wheel cameras captured wheel entry and exit angles. Through image processing, the onboard wheel cameras give the authors the wheel entry and exit angles θ_1 and θ_2 and can also give the wheel sinkage z.

4) OptiTrack Motion Capture: The OptiTrack system provided rover 3 degrees of freedom pose and quaternion orientation at ≈ 120 Hz, giving a file size of ≈ 1 MB, with a mean calibration error of 0.5 mm. The cameras operate at a capture rate of 360 Hz and a resolution of 2048×1088 pixels, providing a calibrated mean positional error of 0.5 mm. The OptiTrack system can be used to get rover speed and subsequently wheel linear speed v.

5) LiDAR Scans of the Testbed: Overhead LiDAR scans capture surface variance at the beginning and end of each trial. Each 20 s scan produces a file that is 700 MB. Plane-fitting on a median stack of a flat ChArUco calibration target yielded a root-mean-square error (RMSE) of 7 mm. The LiDAR scans also give the authors a second way to determine the wheel sinkage z.

C. Coordinate Frames & Transformations

The goal of this subsection is to define all frames in which the sensors are measured, and to describe the transformations required to express all measurements in a common frame for the final data product. The authors collect raw data of position and quaternion information in the OptiTrack Frame $({}^{O}\vec{p},\, {}^{O}\vec{q})$ shown in Fig. 4. Angular velocity and specific force in the IMU Frame $({}^{I}\vec{\omega},\, {}^{I}\vec{f})$ shown in Fig. 1. Encoder data in the wheel frames $({}^{W_i}I,\, {}^{W_i}\theta,\, {}^{W_i}\omega)$ shown in Fig. 1. LiDAR point clouds in the LiDAR frame $({}^{L_\ell}\vec{p}^{j})$ shown in Fig. 4. The final data product is presented in the Trial Frame $({}^{T}\vec{v})$, which is defined as a path-aligned frame such that the initial heading of the rover lies along the $\hat{\mathbf{x}}$ axis. This frame allows all trials, over multiple days of testing and different initial sensor-frame conditions, to be collapsed into a common reference frame for direct comparison.

1) Frame Definitions: Frame definitions are described below; each frame has its name in bold first, the figure reference to visualize the frame second, and ends with the description of the reference frame.

- **OptiTrack Frame (O):** Figure: 4. OptiTrack world reference frame, defined during calibration, sets the origin and axis directions ${}^{O}(\hat{\mathbf{x}}, \hat{\mathbf{y}}, \hat{\mathbf{z}})$ for all tracked objects. In testing, $\hat{\mathbf{z}}$ was set parallel to gravity, $\hat{\mathbf{x}}$ varied slightly day to day, and $\hat{\mathbf{y}}$ followed the right-hand rule.
- **IMU Frame (I):** Figure: 1. Rigidly fixed to the rover frame, displaced from the rover COM by $\vec{r}_I = \left[179.6,\, -54.67,\, 70.88\right]^\top$ mm. Mounting gave $\hat{\mathbf{y}}_I$ aligned with $\hat{\mathbf{x}}_R$, and $\hat{\mathbf{z}}_I$ aligned with $\hat{\mathbf{z}}_R$, with a small tilt about $\hat{\mathbf{z}}$.
- **Each Wheel's Frames (W_i):** Figure: 1. Each has $\hat{\mathbf{x}}$ along forward rolling direction, $\hat{\mathbf{z}}$ normal to terrain, $\hat{\mathbf{y}}$ by the right-hand rule, and origin at the wheel hub.
- **LiDAR Frames (L_ℓ):** Figure: 4. Body fixed, non inertial frame, for each LiDAR in the overhead configuration (denoted with subscript ℓ) is described with $\hat{\mathbf{z}}$ along the optical axis of the color sensor, with $\hat{\mathbf{x}}$ along the direction of increasing index for the columns of the focal plane, and $\hat{\mathbf{y}}$ along the direction of increasing index for the rows of the focal plane. The center LiDAR $\hat{\mathbf{z}}$ is *approximately* aligned with the gravity vector, though not co-linear.
- **Rover Frame (R):** Figure: 1. Body-fixed, non-inertial frame with $\hat{\mathbf{x}}$ forward, $\hat{\mathbf{z}}$ upward, $\hat{\mathbf{y}}$ by the right-hand rule, and origin at rover COM.
- **Trial Frame (T):** Figure: 5. Path aligned frame where the rover starts at $(0, 0, 0)$, initial heading along $\hat{\mathbf{x}}_T$, $\hat{\mathbf{z}}_T$ upward, $\hat{\mathbf{y}}_T$ left.

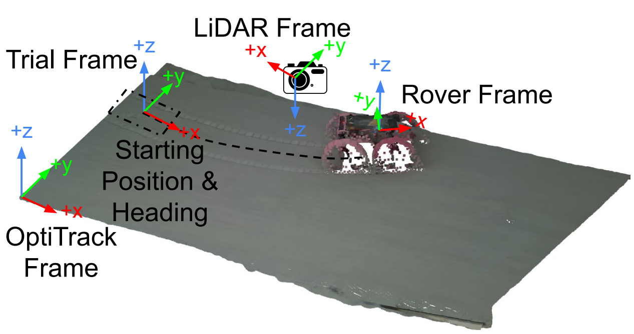

Fig. 5. A point cloud reconstruction of the prepared surface area is shown in this Figure with 4 of the reference frames. The Trial frame is shown to be located at the start of the rover's movement; data from the other three reference frames can be transformed into the trial frame, such that multiple trials can be compared. In this depiction, the headings of the LiDAR frame, rover frame, and OptiTrack frame are arbitrary and can change between trials, but their transformation is known. The trial frame will always be a path aligned frame where the rover starts at $(0, 0, 0)$, initial heading along $\hat{\mathbf{x}}_T$, $\hat{\mathbf{z}}_T$ upward, $\hat{\mathbf{y}}_T$ left.

2) Transformation Matrices: The constant alignment ${}^{T}R^{O}$ is constructed by first defining the upward unit vector $\hat{\vec{u}} = [0,\, 0,\, 1]^\top$. The rover's initial forward direction in the OptiTrack frame is obtained as $\vec{f} = R_{wb}(0)\, [1,\, 0,\, 0]^\top$ and is projected onto the horizontal plane by removing its vertical component, $\tilde{\vec{f}} = \vec{f} - (\vec{f} \cdot \hat{\vec{u}})\, \hat{\vec{u}}$. This projected vector is normalized to yield $\hat{\vec{x}} = \tilde{\vec{f}}/\|\tilde{\vec{f}}\|$, after which $\hat{\vec{z}}$ is set equal to $\hat{\vec{u}}$ and $\hat{\vec{y}}$ is obtained as the cross product $\hat{\vec{y}} = \hat{\vec{z}} \times \hat{\vec{x}}$. The constant trial-to-OptiTrack rotation is then formed as ${}^{T}R^{O} = [\hat{\vec{x}}\ \hat{\vec{y}}\ \hat{\vec{z}}]$.

The IMU-to-rover transformation ${}^{R}T^{I}$ consists of the constant rotation ${}^{R}R^{I}$ and the fixed lever arm $\vec{r}_I$ from the rover's center of mass to the IMU origin, expressed as

$$ {}^{R}T^{I} = \begin{bmatrix} {}^{R}R^{I} & \vec{r}_I \\ \mathbf{0}^\top & 1 \end{bmatrix}, \quad {}^{R}R^{I} = R_{\text{tilt}}\, R_{90} \tag{2} $$

where R_{tilt} accounts for the small out-of-plane tilt during mounting and R_{90} aligns the IMU axes to the rover coordinate convention. Similarly, each wheel frame W_i is related to the rover frame by the fixed transformation

$$ {}^{R}T^{W_i} = \begin{bmatrix} {}^{R}R^{W_i} & \vec{r}^{W_i} \\ \mathbf{0}^\top & 1 \end{bmatrix} \tag{3} $$

where ${}^{R}R^{W_i}$ is the constant rotation from wheel frame to rover frame and $\vec{r}^{W_i}$ is the translation from the rover's center of mass to the wheel hub.

The rover-to-trial transformation ${}^{T}T^{R}(k)$ is time-varying, incorporating both the instantaneous rover pose in the OptiTrack frame and the constant alignment ${}^{T}R^{O}$. It is expressed as

$$ {}^{T}T^{R}(k) = \begin{bmatrix} {}^{T}R^{R}(k) & {}^{T}\vec{p}^{R}(k) \\ \mathbf{0}^\top & 1 \end{bmatrix} \tag{4} $$

with

$$ {}^{T}R^{R}(k) = {}^{T}R^{O}\, {}^{O}R^{R}(k), \tag{5} $$

$$ {}^{T}\vec{p}^{R}(k) = {}^{T}R^{O} \left({}^{O}\vec{p}^{R}(k) - {}^{O}\vec{p}^{R}(0) \right). \tag{6} $$

This definition ensures that the rover's initial pose coincides with the trial frame origin and that the initial heading aligns with $\hat{\mathbf{x}}_T$.

The OptiTrack-to-trial transformation is fixed for each trial and determined from the rover's initial pose in the OptiTrack frame:

$$ {}^{T}T^{O} = \begin{bmatrix} {}^{T}R^{O} & -\,{}^{T}R^{O}\, {}^{O}\vec{p}^{R}(0) \\ \mathbf{0}^\top & 1 \end{bmatrix}. \tag{7} $$

This mapping removes the initial translation and rotates the OptiTrack axes so the rover's initial forward direction aligns with $\hat{\mathbf{x}}_T$.

To unify the LiDAR frame L_ℓ with the OptiTrack frame, a static transformation ${}^{O}T^{L_\ell}$ is computed using a calibration target. Given the pose of the target in the OptiTrack frame ${}^{O}T^{C}$, the pose of the same target in the LiDAR frame ${}^{L_\ell}T^{C}$ (estimated via OpenCV's ChArUco detection), and the known intermediate translation ${}^{C}r$ from the calibration target rigid body origin to the estimated pose origin, the LiDAR-to-OptiTrack transformation is

$$ {}^{O}T^{L_\ell} = {}^{O}\, T^{C} \begin{bmatrix} \mathbf{I} & -{}^{C}r \\ \mathbf{0} & 1 \end{bmatrix} \left({}^{L_\ell}T^{C} \right)^{-1}. \tag{8} $$

This calibration is repeated for each LiDAR used during a day of trials so that all LiDAR point clouds can be expressed in a common OptiTrack frame. When transforming LiDAR data into the trial frame, the static transformation ${}^{O}T^{L_\ell}$ is combined with ${}^{T}T^{O}$, giving the time-dependent LiDAR-to-trial mapping

$$ {}^{T}T^{L_\ell}(k) = {}^{T}T^{O}(k)\,{}^{O}T^{L_\ell}. \tag{9} $$

3) Applying the Transformations: OptiTrack motion capture data, which provide the rover's position and orientation in the OptiTrack frame, are expressed in the trial frame by subtracting the initial position and applying the fixed rotation ${}^{T}R^{O}$. The transformation for positions is

$$ {}^{T}\vec{p}^{O}(k) =,{}^{T}R^{O}\big(,{}^{O}\vec{p}(k) -,{}^{O}\vec{p}(0)\big), \tag{10} $$

while orientations are mapped by

$$ {}^{T}R^{R}(k) =,{}^{T}R^{O},{}^{O}R^{R}(k), \qquad {}^{T}q^{R}(k) = q_{tw},\otimes,q_{wb}(k), \tag{11} $$

where q_{tw} is the quaternion representation of ${}^{T}R^{O}$, $q_{wb}(k)$ corresponds to ${}^{O}R^{R}(k)$, and the quaternion product is ordered to map orientations from the rover frame to the trial frame.

Wheel sensor measurements are handled according to type. Encoder angles and rates are expressed using the sign convention aligned with $\hat{\mathbf{x}}_R$. When a wheel angular velocity vector is required in the trial frame, the transformation applies both the constant wheel-to-rover rotation and the time-varying rover-to-trial rotation:

$$ {}^{T}\vec{\omega}^{W_i}(k) =,{}^{T}R^{R}(k),{}^{R}R^{W_i},{}^{W_i}\vec{\omega}(k). \tag{12} $$

For the IMU measurements, both angular velocity and specific force are treated as vectors and require only rotational transformation into the trial frame. Using the time-varying rotation ${}^{T}R^{R}(k)$ from the rover frame to the trial frame and the constant extrinsic rotation ${}^{R}R^{I}$ from the IMU to the rover frame, the mappings are given by

$$ {}^{T}\vec{\omega}(k) =,{}^{T}R^{R}(k),{}^{R}R^{I},{}^{I}\vec{\omega}(k), \tag{13} $$

$$ {}^{T}\vec{f}(k) =,{}^{T}R^{R}(k),{}^{R}R^{I},{}^{I}\vec{f}(k). \tag{14} $$

Linear acceleration is recovered from the IMU specific force measurement by accounting for the lever arm $\vec{r}I$ and rotational effects according to

$$ \vec{a}_{\text{origin}} = \vec{f} + \dot{\vec{\omega}} \times \vec{r}_I + \vec{\omega} \times (\vec{\omega} \times \vec{r}_I). \tag{15} $$

LiDAR point cloud data are transformed using the LiDAR-to-trial frame mapping ${}^{T}T^{L_\ell}$ from Eq. 9. Each point ${}^{L_\ell}\vec{p}^{j}$ in LiDAR coordinates is mapped to the trial frame through the standard homogeneous transformation chain from L_ℓ to T.

D. Processed Data Results

In this section, each timeseries of the rover's state and action is generated from the sensors into a reference frame intended for characterizing rover mobility. Motion capture, IMU data processed into rover state timeseries is presented,

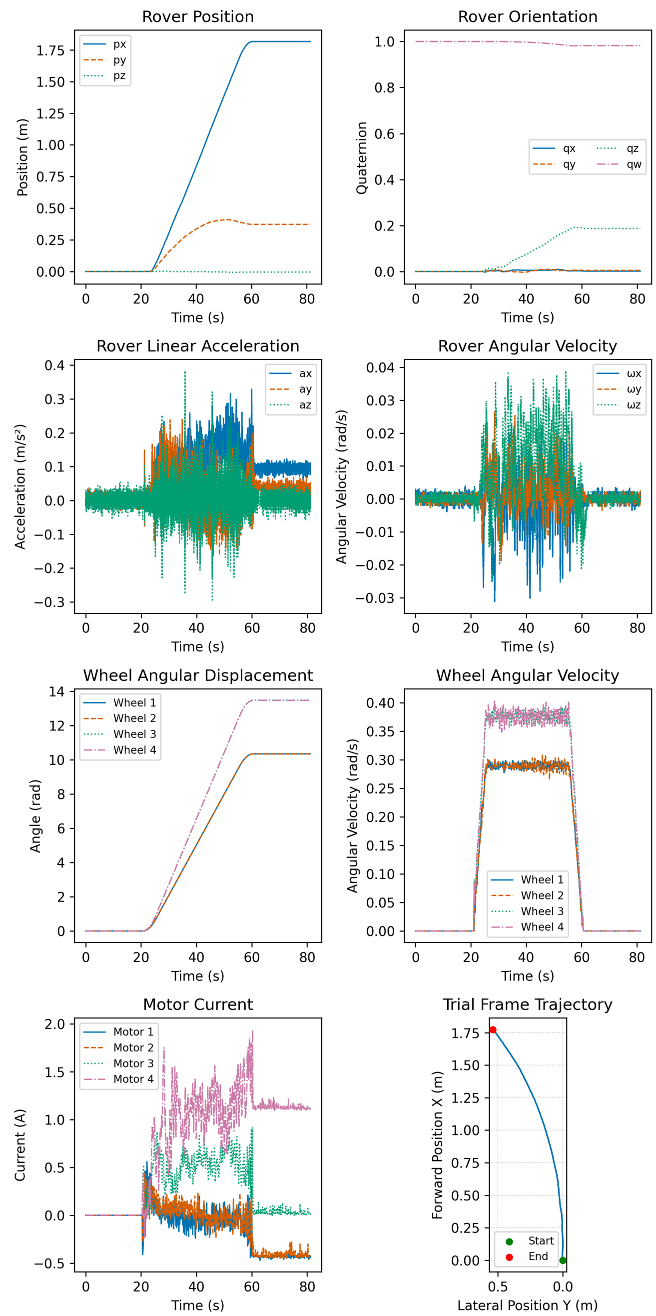

Fig. 6. Combined overview of rover position, orientation, linear acceleration, angular velocity, wheel angular displacement, wheel angular velocity, motor current, and trial frame trajectory for a trial conducted at a linear speed of 5 cm/s, a 120 cm radius counter-clockwise turn, and a 0° inclination. All sensor measurements were post-processed to remove bias and noise and transformed into the trial frame for consistent comparison.

and encoder data processed into control input timeseries is shown in Fig. 6.

A still frame of wheel camera videos is presented in Fig. 7. Lastly, a comparison between two LiDAR scans is presented in Fig. 8. Each timeseries pairs with environment data, such as slope inclination, initial surface topography, and final surface topography, generated from medians of LiDAR scan data from before and after each trial, and each wheel's camera video. To assist in describing the processing steps, frame transformations, and interpreting these results, each sensor's data post-processing is described for a trial with linear speed of 5 cm/s, an 120 cm radius turn (counter-clockwise turn), on a 0° inclination. Additionally, the code used to post-process the data is available in the GitHub repository. The available open source data can be reprocessed to support a research group's needs or used directly as presented.

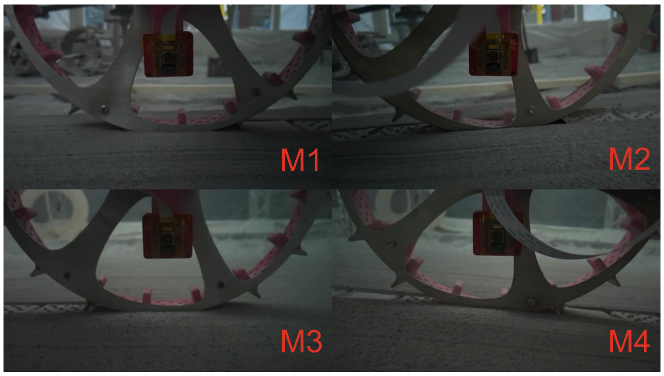

Fig. 7. Wheel camera video still frame of a trial with linear speed of 5 cm/s, an 120 cm radius turn (counter-clockwise turn), on a 0° inclination. In clockwise order, starting with the top left, are the front left, back left, front right, and back right wheels.

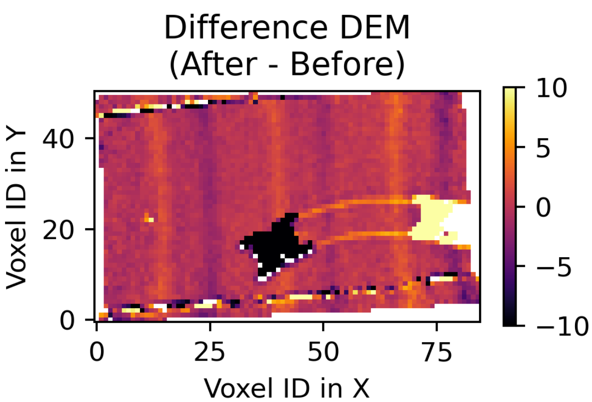

Fig. 8. Example comparison between the digital elevation maps (DEMs) constructed from scans before and after a trial with linear speed of 5 cm/s, an 120 cm radius turn (counter-clockwise turn), on a 0° inclination. Notice the visible tread impressions from the rover path. Note that the sinusoidal banding seen in the residual is an artifact of the median filtering process, and originates from interference from the similar optical band-pass of the motion capture and lidar systems and their emitting and capture frequencies, respectively.

E. Off-Nominal Data

During the experimentation campaign, some trials had "hiccups". Sensors did not start, scans were incomplete, mechanical issues, and placing the RoSEy in the wrong position are some examples of problems that arose in testing. If a trial had "off-nominal data," it was repeated, but that data was not deleted; it was moved to a section labeled Off-Nominal Data. This data may or may not be useful, and the exact cause of why it is not included in the main dataset is not labeled, but it is available for researchers to use.

V. Conclusion

This work introduced a complete experimental pipeline for measuring rover mobility on granular terrain and presented a public dataset comprising 1680 controlled trials conducted with the RoSEy CubeRover in the MLSS facility. The methodology combined synchronized onboard telemetry, motion-capture ground truth, and overhead LiDAR terrain scans, yielding tightly registered measurements suitable for both physics-based and data-driven traversability studies. The accompanying open-source tools streamline data post-processing and integration into simulation environments.

By releasing these resources, the paper lowers the barrier to rigorous terramechanics research and provides a common benchmark for identifying mobility models, perception algorithms, and autonomy frameworks. Future work will extend the dataset to include variable wheel designs, heterogeneous soil conditions, and dynamic loading profiles, further enriching the community's ability to predict and enhance rover performance on planetary surfaces.

Acknowledgment

This work involved many hours in the heat and dust, and was made possible by the combined efforts of the authors and the following undergraduate students: Emma Bowden, Quinn Caldwell, Ryan Manley, Ainsley Soleta, Aidan Staszak, and Waylon Weeks.

References

[1] B. C. Hopkins and F. Zhu, "Uncertainty quantification & sensitivity analysis of parameters impacting rover dynamics," submitted, under review at *Journal of Terramechanics*.

[2] K. A. Johnson, V. M. Asnani, J. Polack, and M. Plant, "Experimental evaluation of the scale model method to simulate lunar vehicle dynamics," in *Proceedings of the International Society for Terrain–Vehicle Systems (ISTVS) Americas Regional Conference*, no. GRC–E–DAA–TN32423. Detroit, MI, USA: International Society for Terrain–Vehicle Systems, Sep. 2016, pp. 1–17. [Online]. Available: https://ntrs.nasa.gov/citations/20170000950

[3] P. Bartlett, D. Wettergreen, and W. R. L. Whittaker, "Design of the scarab rover for mobility and drilling in the lunar cold traps," in *Proceedings of 9th International Symposium on Artificial Intelligence, Robotics and Automation in Space (iSAIRAS '08)*, February 2008.

[4] M. Ono, M. Heverly, B. Rothrock, E. Almeida, F. Calef, T. Soliman, N. Williams, H. Gengl, T. Ishimatsu, A. Nicholas, E. Stilley, K. Otsu, R. Lange, and S. M. Milkovich, "Mars 2020 Site-Specific Mission Performance Analysis: Part 2. Surface Traversability," in *2018 AIAA SPACE and Astronautics Forum and Exposition*. Orlando, FL: American Institute of Aeronautics and Astronautics, Sep. 2018. [Online]. Available: https://arc.aiaa.org/doi/10.2514/6.2018-5419

[5] Astrobotic Technology, "Cuberover," https://www.astrobotic.com/lunar-delivery/rovers/cuberover/, 2025, accessed 9 May 2025.

[6] I. E. Jehn, B. Dreyer, C. Johnson, and P. Lee, "Implications of Lunar Simulant Geotechnical Properties on Testbed Experimentation and Engineering Analysis and Reported Properties of Colorado School of Mines Highland Simulant," submitted, under review at *Space and Planetary Resources*.

[7] C. Creager, V. Asnani, H. Oravec, and A. Woodward, "Drawbar pull (dp) procedures for offroad vehicle testing," NASA Glenn Research Center, Cleveland, OH, USA, NASA Technical Publication NASA/TP–2017–219384, Aug. 2017. [Online]. Available: https://ntrs.nasa.gov/citations/20170010706